Int J Adv Manuf Technol (2015) 78:1371–1380
DOI 10.1007/s00170-014-6749-8

ORIGINAL ARTICLE

Analytical and numerical studies of fatigue stresses in friction stir welding

Z. Zhang · Q. Wu

Received: 8 July 2014 / Accepted: 19 December 2014 / Published online: 9 January 2015

Abstract Computational fluid dynamic model of the friction stir welding process was established. Forces acting on the welding tool were computed according to the obtained pressure fields. The obtained transverse force on the welding tool can be validated by comparison of both experimental and numerical results in published literatures. Analytical methods for the calculation of the fatigue stresses on the welding tool were then proposed. The analytical methods were compared to the finite element model for validations. Results indicate that the frictional force on the shoulder contact surface takes the main contribution to the transverse force on the welding tool. The maximum fatigue stress on the pin is decreased with the increase of the rotating speed and increased with the increase of the transverse speed.

Keywords Friction stir welding · Eulerian model · Fatigue stress · Tool force

1 Introduction

As a solid state joining technology invented by Thomas et al. [1], friction stir welding (FSW) has revealed its advantages in comparison to the traditional fusion welding technologies. FSW has been quickly applied to many industries including aerospace, ship manufacturing, train manufacturing, etc. [2, 3].

In FSW, the rotating tool is inserted to the joining line of the welding plates. With rotations and longitudinal movements, the material near the joining line can be mixed and then a tight joint can be formed. In this process, the welding tool is the key component for the success of the welding. Çam et al. [4, 5] reported the microstructures of the welding zones and the mechanical properties of the joints in various FSW processed aluminum alloys. The effects of the pin length and diameters on the tool forces have been studied by Sorensen et al. [6]. It shows that the tool force in the longitudinal direction measured by dynamometer is increased with the increase of the pin length. Kumar et al. [7] utilized the systematic experimental design method to investigate the heat input and the tool forces in the friction stir welding of AA5083. By the use of the measuring method based on the input electrical signatures of the driving motors, the torque and the tool force data during FSW were captured by Mehta et al. [8]. By the use of a rotating component dynamometer and a finite element model, the tool forces for different welding parameters are analyzed by Trimble et al. [9]. Balasubramanian et al.[10] measured the process force in FSW of AA6061-T6 by a high-frequency data acquisition system.

Besides of the experimental methods, numerical method can provide a detailed insight into the mechanism on tool forces with lower research costs. Carlone et al. [11] analyzed the influence of process parameters on microstructure and mechanical properties in AA2024-T3 FSW by both numerical model and experimental tests. By an adaptive remeshing technique based on FE model, Zhang et al. [12] studied the tool forces in three directions during friction stir welding of AZ91. Ulysse [13] developed a 3D viscoplastic model to simulate the butt joints of friction stir welded aluminum thick plates. The force acting on the pin is further discussed. DebRoy et al. [14] created a 3D heat and mass flow model, and implemented it into a fast calculation algorithm. Then, tool durability maps with various welding variables were generated. By using a similar 3D heat transfer and viscoplastic material flow model, Arora et al. [15] computed the transverse

Z. Zhang (✉) · Q. Wu
Department of Engineering Mechanics, State Key Laboratory of Structural Analysis for Industrial Equipment, Faculty of Vehicle Engineering and Mechanics, Dalian University of Technology, Dalian 116024, China
e-mail: zhangz@dlut.edu.cn

force and torque during friction stir welding. The computed values were used to analyze the shear stress experienced by the tool pin due to bending and torsion under different welding parameters. Soundararajan et al. [16] predicted the stress at the workpiece and backplate interface by a FE thermomechanical model. A fully coupled thermomechanical model was developed by Zhang et al. [17] to study the material deformations and heat generations in FSW, and then the effect of tool sizes and shapes was investigated [18]. Assidi et al. [19] developed a 3D FE model based on an Arbitrary Lagrangian Eulerian (ALE) formulation, and the influences of the different friction models on the vertical and the transverse forces were studied.

Although many useful experimental methods and interesting numerical models have been used for the determination of the tool forces, the force distribution on the tool has not been studied in detail. Moreover, the computational methods on the fatigue stress of the tool have not been reported. So, a Computational Fluid Dynamics (CFD) model is developed in current work for the determination of the tool forces and the force distributions on the welding tool. The obtained forces are compared to the experimental tests in published literatures for validations. Then, two new analytical methods are proposed for the calculations of the fatigue stress on the welding tool. The finite element model is used to validate the proposed analytical methods.

2 Model description

2.1 CFD model for prediction of tool force

The schematic model of the welding plate is shown in Fig. 1. The dimension of the plate is 200×120×7 mm. The tool geometry is shown in Fig. 2. The material of the welding plate is AA6061-T6. The thermal and mechanical properties of AA6061-T6 are functions of temperatures, as shown in Table 1 [20, 21].

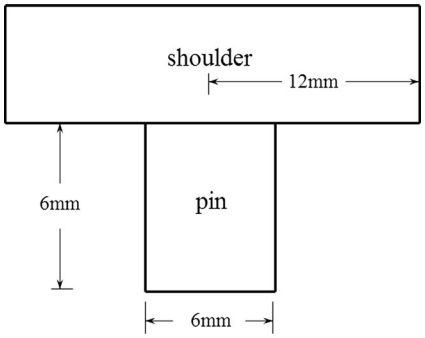

Fig. 2 Geometry of welding tool

In the CFD model, viscosity of the fluid can be obtained as follows [22],

$$\mu = \frac{\overline{\sigma}_s}{3\dot{\overline{\varepsilon}}} \tag{1}$$

where μ is the viscosity of fluid, $\overline{\sigma}_s$ is the flow stress of the material $\overline{\sigma}_s = \sqrt{\frac{3}{2}\sigma : \sigma}$ [23], and $\dot{\overline{\varepsilon}}$ is the equivalent strain rate of the deformed material. In order to simplify the calculation, the strain rate in the fluid field is calculated base on the velocity distribution [24]:

$$\dot{\varepsilon} = \frac{1}{2}\left(\nabla \mathrm{v} + \nabla \mathrm{v}^{\mathrm{T}}\right) \tag{2}$$

The velocity of the material at the contact surface v_s is calculated:

$$v_s = \delta \omega r \tag{3}$$

where ω is the rotating speed of the tool, r denotes the distance from the rotating axis, δ is the slipping factor and set to be 0.5. The transverse speed of the tool is represented by the velocity inlets. The outlet is set as a pressure-free outlet. According to literatures [16, 25], the axis force F is set to be 15 kN during

Fig. 1 Schematic of FSW plate

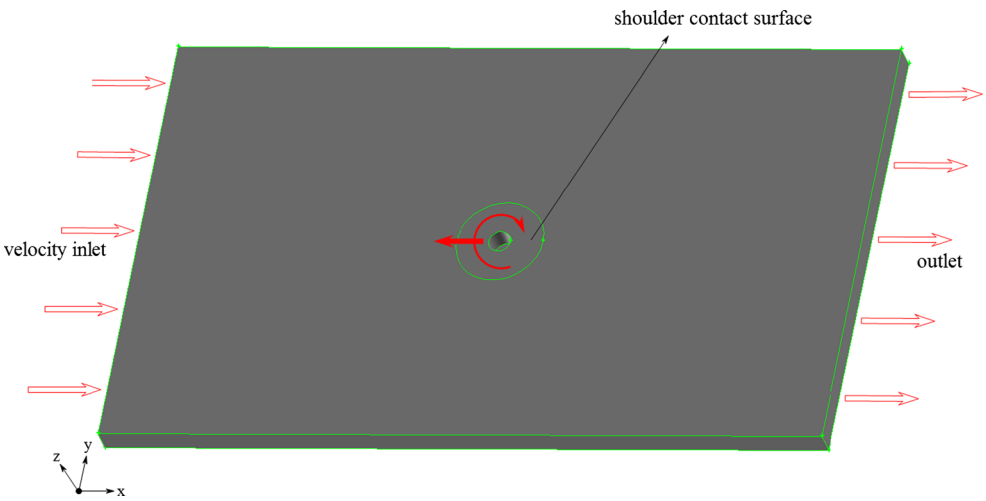

Table 1 Thermal properties of AA6061-T6 [20, 21]

Temperature (K)	Specific heat (J/kg·K)	Conductivity (W/m·K)	Flow stress (MPa)	Poisson's ratio
273	917	162	277.7	0.23
366	978	177	264.6	
477	1024	192	218.6	
588	1078	207	66.2	
700	1133	223	17.9	

the calculation. At the top surface, the heat convection coefficient is defined to be 100 W/m^2·K.

The temperature distribution is important during FSW. During the welding process, the heat is generated from the shoulder and the pin contact surfaces. In current model, the heat input is simplified as the heat flux sources on the shoulder contact surface and the pin side and tip surfaces according to [26]. The heat input power can be then calculated from the work done by frictional force.

At the shoulder contact surface, the frictional force on the area element could be defined as:

$$df_{\text{shoulder}} = \min\left(\frac{\mu_{\text{f}} F}{S_{\text{shoulder}}}, \tau_{\max}\right) \cdot ds \tag{4}$$

where S_{shoulder} is the area of the shoulder surface and $\tau_{\max}$ is the maximum shear stress [23]:

$$\tau_{\max} = \frac{\overline{\sigma}_{\text{s}}}{\sqrt{3}} \tag{5}$$

ds represents the area of the element and μ_{f} is the friction coefficient and can be calculated by [27, 28]:

$$\mu_f = \mu_0 \exp\left(-\delta \frac{\omega}{\omega_0} \frac{r_{\text{p}}}{R_{\text{s}}}\right) \tag{6}$$

where μ_0 is the static friction coefficient and here is taken as 0.45 [29, 30]. ω is the rotating speed and the reference rotation speed ω_0 is taken as 400 rpm. r_{p} and R_{s} are the radii of the tool pin and the shoulder, respectively. The heat input power on the area element can be obtained:

$$dP = 2\pi r \frac{\omega}{60} df_{\text{shoulder}} \tag{7}$$

Then, the total heat input power of the shoulder can be calculated by the integral of Eq. (7):

$$P_{\text{shoulder}} = \int_S dP \tag{8}$$

In current model, the above equation can be simplified as:

$$P_{\text{shoulder}} = \sum_{i=1}^{n_{\text{s}}} 2\pi r_{\text{i}} \frac{\omega}{60} df_{\text{shoulder}} \tag{9}$$

where n_{s} is the total number of area element on the shoulder contact surface. The heat flux on the shoulder-plate contact interface can be then obtained according to [23]:

$$q_{\text{shoulder}} = \frac{P_{\text{shoulder}}}{S_{\text{shouler}}} \tag{10}$$

Similar to Eq. (4), the frictional force at pin side and tip surface can be defined as:

$$df_{\text{pin}} = \min(\mu_{\text{f}} p, \tau_{\max}) \cdot ds \tag{11}$$

where p is the calculated normal pressure on the pin surface. Then heat input power of the pin can be computed:

$$P_{\text{pin}} = \sum_{i=1}^{n_{\text{p}}} 2\pi r_{\text{i}} \frac{\omega}{60} df_{\text{pin}} \tag{12}$$

where n_{p} is the total number of area element on the pin contact surface. The heat flux on the pin-plate contact interface can be then obtained according to [23]:

$$q_{\text{pin}} = \frac{P_{\text{pin}}}{S_{\text{pin}}} \tag{13}$$

where S_{pin} is the area of the pin surface.

The total heat flux at interfaces in this model is given by:

$$q_{total} = q_{\text{shoulder}} + q_{\text{pin}} \tag{14}$$

User defined functions compiled by C language were used to define the material properties and heat generation in current CFD model. Seven cases for different rotating and transverse speeds were simulated, as shown in Fig. 3.

2.2 Analytical methods for prediction of fatigue stress

Figure 4a shows the tip force acting on the pin. The diameter of the pin is identical to the length of the pin. So, the Timoshenko beam theory [31] instead of the Eulerian beam theory [32] should be applied for the calculation of the fatigue stress on the welding tool. The tool pin can be simplified as a cantilever in the Timoshenko beam

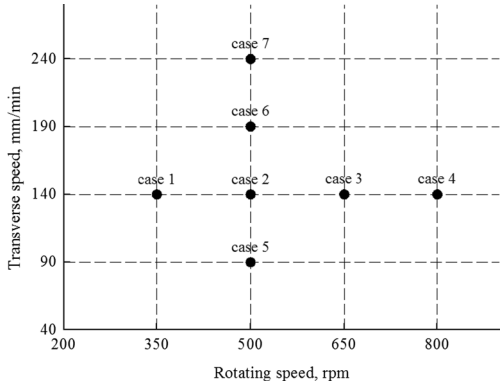

Fig. 3 Welding parameters for seven cases

theory. The in-plane bending elasticity problem can be treated as the solution to the biharmonic equation [33]:

$$\frac{\partial^4\phi}{\partial x^4}+2\frac{\partial^4\phi}{\partial x^2\partial y^2}+\frac{\partial^4\phi}{\partial y^4}=0 \tag{15}$$

where ϕ is the stress function in Cartesian coordinates and ϕ follows the relations as follows:

$$\begin{cases}\sigma_x=\dfrac{\partial^2\phi}{\partial y^2}\\ \sigma_y=\dfrac{\partial^2\phi}{\partial x^2}\\ \tau_{xy}=-\dfrac{\partial^2\phi}{\partial x\partial y}\end{cases} \tag{16}$$

The stress function can be chosen as [33]:

$$\phi=C_5xy^3+C_6xy \tag{17}$$

The boundary conditions can be shown as:

$$\begin{cases}(\tau_{\mathrm{xy}})_{y=\pm R}=0\\ \int_{\mathrm{sec}}(\tau_{\mathrm{xy}})_{x=0}ds=-F_{\mathrm{tip}}\end{cases} \tag{18}$$

Then the stress of the pin can obtained from solving Eqs. (15) to (18):

$$\sigma_x=-\frac{8}{3}\frac{F_{\mathrm{tip}}}{\pi R^4}xy \tag{19}$$

The normal pressure on the pin side surface can lead to the pin force F_{pin}. Two different analytical methods can be used to compute the fatigue stress on the pin.

In analytical method 1, it is assumed that the pin force is equivalent to a uniform linear load on the top surface of the pin, and the solution is also an in-plane problem, as show in Fig. 4b. The stress function satisfies Eqs, (15)–(16).

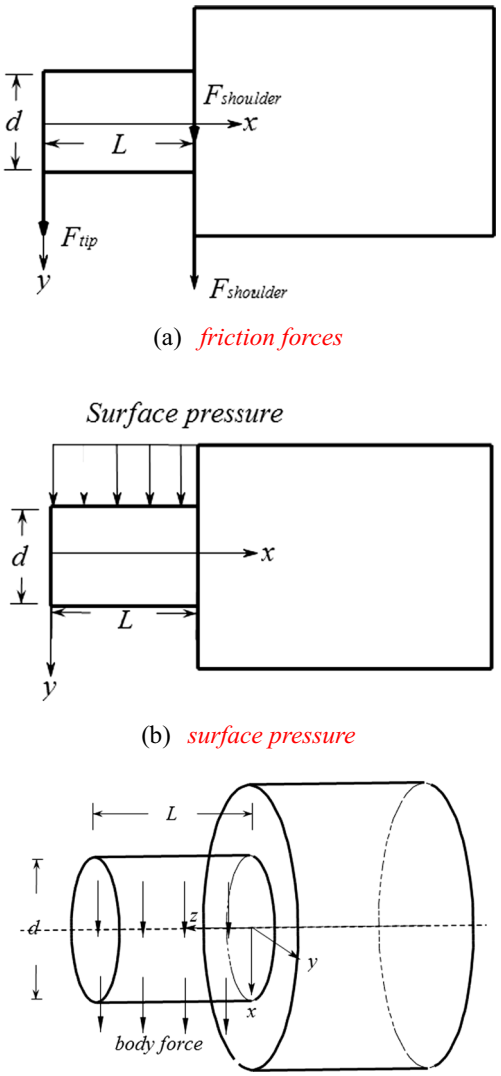

Fig. 4 Schematic of pin loads. **a** Friction forces **b** sruface pressure and **c** body force

σ_y is the function of y:

$$\sigma_{\mathrm{y}}=f(y) \tag{20}$$

Then, the stress function can be determined by integration of Eq. (20):

$$\phi=\frac{1}{2}x^2f(y)+xf_1(y)+f_2(y) \tag{21}$$

where f_1 and f_2 are arbitrary functions.

The force boundary conditions are:

$$\begin{cases}(\sigma_{\mathrm{y}})_{y=-\frac{d}{2}}=\sigma_{\mathrm{q}}\\ (\sigma_{\mathrm{y}})_{y=\frac{d}{2}}=(\tau_{\mathrm{xy}})_{y=\pm\frac{d}{2}}=0\end{cases} \tag{22}$$

where σ_q is the stress in y-direction caused by the distributed load. Due to the concentrated linear loads on the top surface of

the pin, a surface shown in Fig. 5 is used for simplification of the calculations. r is taken as 0.9 R in the calculation as an engineering approximation.

Force and moment equilibrium equations on the cross sections should be satisfied:

$$\begin{cases} \int_{\text{sec}} (\tau_{xy})_{x=L} ds = 0 \\ \int_{\text{sec}} y(\sigma_x)_{x=L} ds = 0 \\ (\tau_{xy})_{x=0} = 0 \end{cases} \tag{23}$$

where *sec* represents the circular cross section of the pin. A four-order polynomial stress function is used. By the solution to the above equations, the stresses caused by the uniform pressure on the top surface are:

$$\begin{cases} \sigma_x = 3x^2 C_1 y - 2C_1 y^3 + 6C_2 y \\ \sigma_y = C_1 y^3 + C_3 y + C_4 \\ \tau_{xy} = -x\left(3C_1 y^2 + C_3\right) \end{cases} \tag{24}$$

where the constants are:

$$\begin{cases} C_1 = \dfrac{-F_{\text{pin}}}{2L\sqrt{R^2 - r^2}\left(2R^3 + 3rR^2 - r^3\right)} \\ C_2 = \dfrac{1}{6} C_1 R^2 \\ C_3 = -3C_1 R^2 \\ C_4 = 2C_1 R^3 \end{cases} \tag{25}$$

In analytical method 2, it is assumed that the pin force F_{pin} is equivalent to a uniform distributed body force, as shown in Fig. 4c. This stress caused by the uniform distributed body force can be solved as space elasticity problem. The stress and strain components satisfy the following equations [34]:

$$\begin{cases} \sigma_{ij,i} + F_j = 0 \\ \sigma_{ij} = \lambda\theta\delta_{ij} + 2\mu\gamma_{ij} \end{cases} (i, j = 1, 2, 3) \tag{26}$$

where σ_{ij} are the stress components, γ_{ij} are the strain components, F_j are the body force density, $\theta = \gamma_{ii}$, λ, and μ are Lame constants.

The above functions should satisfy the follow boundary conditions:

$$\begin{cases} F_1 = f_x = \dfrac{F_{\text{pin}}}{V}, F_2 = F_3 = 0 \\ \iint_{\text{tip}} (\tau_{xy}, \sigma_z) ds = 0 \\ \iint_{tip} \sigma_z x ds = 0 \\ (\sigma_{ij})_{\text{side}} = 0 \end{cases} \tag{27}$$

where V is the volume of the pin, tip and side represent the tip surface and side surface of the pin, respectively.

To find the solution of the above equations, the stress and strain are assumed to be the following form:

$$\begin{cases} \sigma_{ij} = \dfrac{1}{2} z^2 \sigma_{ij}^{(2)} + z\sigma_{ij}^{(1)} + \sigma_{ij}^{(0)} \\ \gamma_{ij} = \dfrac{1}{2} z^2 \gamma_{ij}^{(2)} + z\gamma_{ij}^{(1)} + \gamma_{ij}^{(0)} \end{cases} (i, j = 1, 2, 3) \tag{28}$$

where $\sigma_{ij}^{(k)}$ and $\gamma_{ij}^{(k)}$ (k=0,1,2) are functions of x and y. By solving the Eq. (26) with the boundary conditions (27), the stress in z direction of this space elasticity problem can obtained:

$$\sigma_z = -E\left(k_0 + k_1 + \frac{1}{2} k_2 z^2\right) x + \mu k_2 x\left[-\frac{9 + 13v + 6v^2}{3} R^2 + \left(1 + \frac{v}{2}\right)\left(x^2 + y^2\right)\right] \tag{29}$$

where E is the elasticity modulus, v is the Poisson ratio, and k_i (i=0,1,2) are constants:

$$\begin{cases} k_0 = \dfrac{1}{2} k_2 \left[L^2 - \dfrac{9 + 13v + 4v^2}{6(1 + v)} R^2\right] \\ k_1 = -k_2 L \\ k_2 = \dfrac{2F_{pin}}{\mu V (1 + v) R^2} \end{cases} \tag{30}$$

The fatigue stress on the welding pin can be then obtained by the superposition method.

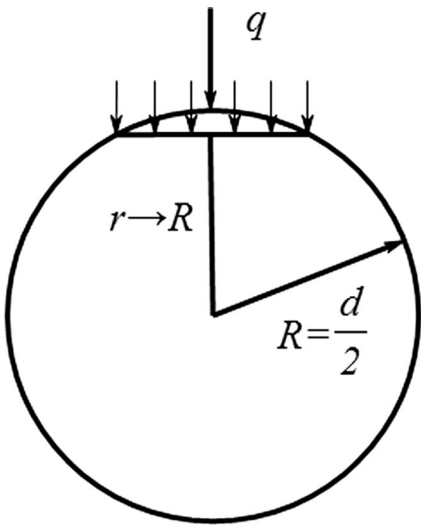

Fig. 5 Boundaries of tool pin in analytical models

Table 2 Thermal properties of AISI A2 steel [35]

Temperature (K)	Thermal expansion (μm/m·K)	Elastic modulus (GPa)	Conductivity (W/m·K)	Specific heat (J/kg·K)
293	11.5	192	–	445
366	12.8	191	51.9	–
423	12.4	189	–	–
473	12.7	186	48.5	–
533	13.1	182	–	–
588	13.7	177	–	–
643	14.0	171	41.5	550

2.3 Finite element model for prediction of fatigue stress

Due to the temperature rises on the welding tool, the mechanical properties of the tool should be considered as the functions of the temperatures. The material of the welding tool is AISI A2 steel. The mechanical properties of AISI A2 steel are shown in Table 2 [35]. During the FSW process, the generated heat on the contact surface can flow into both the welding plates and the welding tool, which can lead to the temperature rises in both the welding plate and the welding tool. In order to compute the temperature rises on the welding tool, a total proportion of 10 % heat input is assumed to be absorbed by the tool according to Ref. [36]. The numerical and experimental temperature rises on the welding tool from Dickerson [37] are used for validations of the current finite element model. The welding parameters and geometry of the tool in the validation model are set to be the same to the experimental tests in [37]. Then, a simplified cylindrical tool was used to study the effect of the welding parameters.

ABAQUS is used to calculate the fatigue stress of the welding tool. During the calculation, the beam was meshed into 40 2D plane Timoshenko beam elements (Fig. 6). The cantilever beam is simplified as a wire with circular section. The applied load consists of a linear load on the wire and a concentrated force on the tip.

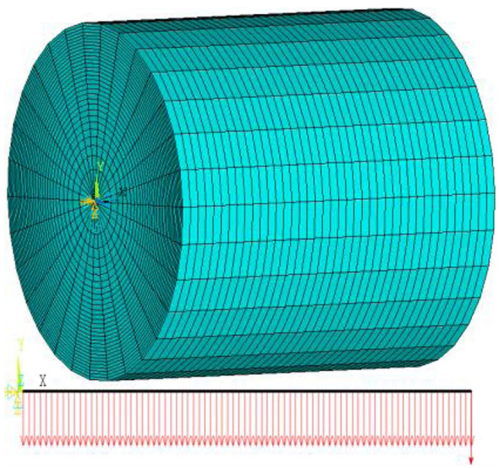

Fig. 6 Finite element model of pin

3 Results and discussions

3.1 Temperature distributions

The calculated temperatures of the simulated cases are shown in Fig. 7. The maximum temperatures appear at the contacting surface of shoulder and tool pin. The contours of temperature are symmetrical to the welding line. As shown in Fig. 7, in cases 1-4, the maximum temperatures are increased with the increase of the rotating speeds. The peak temperature is increased from 670 to 750 K, when the rotating speeds are increased from 350 to 800 rpm. In Fig. 7, in cases 5, 2, 6, and 7, the maximum temperatures are decreased when the transverse speeds are increased. At a transverse speed of 90 mm/min, the peak temperature of the piece is 748 K. When the transverse speed is increased to 240 mm/min in case 7, the maximum temperature is decreased to only 681 K. This phenomenon is mainly due to the much higher heat loss in higher transverse speeds. The variation of the peak temperature with the rotating speeds and the transverse speeds is fitted well with the observations in published literatures [38, 39].

3.2 Tool forces

Figure 8 illustrates the pressure distributions on tool pin in different cases. During the welding process, the materials are

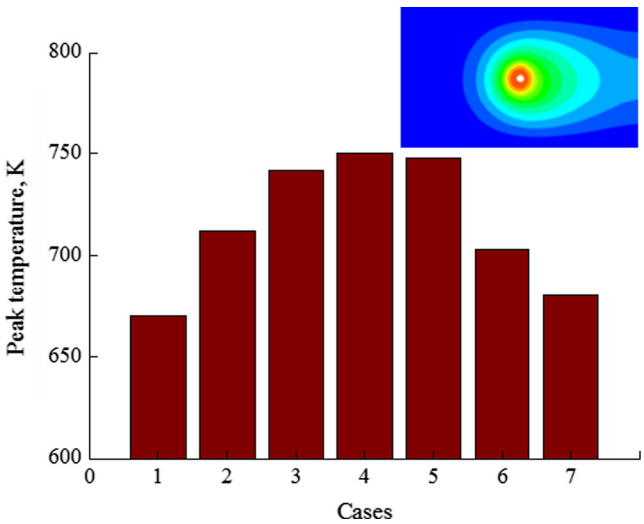

Fig. 7 Temperature histogram of different cases

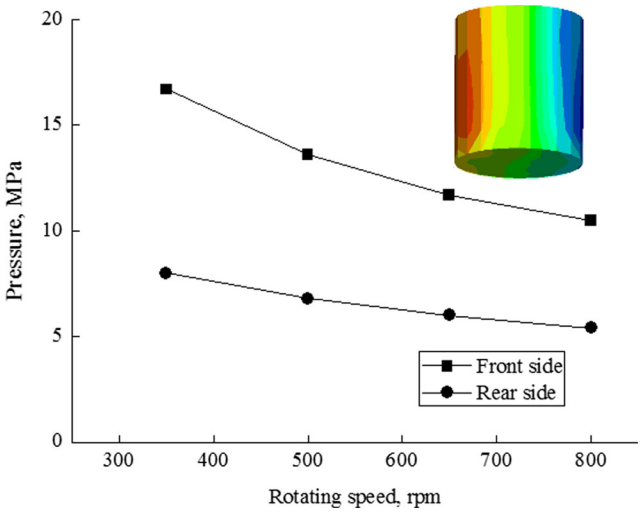

(a) *effect of rotating speed*

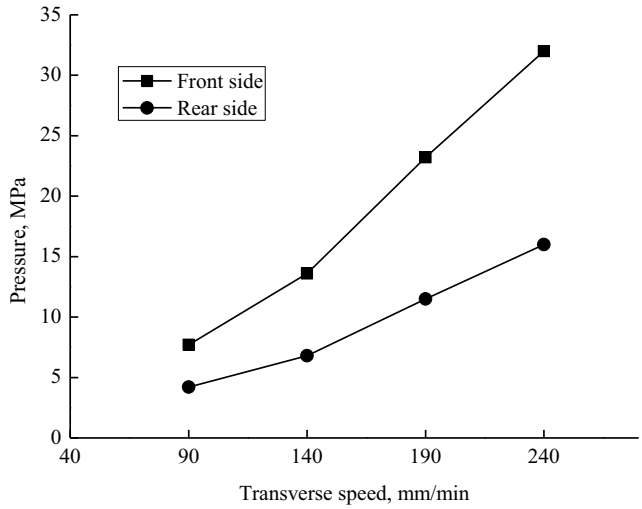

(b) *effect of transverse speed*

Fig. 8 Pressure variations with welding parameters on tool pins. **a** Effect of rotating speed and **b** effect of transverse speed

pressed on the front side of the tool pin, and then flowed around the tool to the rear side. This is the reason that the pressure at the front side of the tool pin is much higher than the one at the rear side. The resistant force on the tool pin is caused by the pressure difference between the front and rear sides of the pin. With the increase of the rotating speeds, the difference of pressure between the two sides is decreased. When the rotating speed is 350 rpm, the pressure difference is 8.95 MPa. When the rotating speed increased to 800 rpm, the pressure difference is decreased to 5.1 MPa. Higher transverse speed can lead to obvious increase of the pressure difference. The pressure difference can be increased from 3.6 to 15.9 MPa when the transverse speed is increased from 90 to 240 mm/min.

The transverse force, i.e., the force in the welding direction, consists of two parts, the frictional force on the shoulder contact surface and the force on the pin:

$$F_x = F_{\text{shoulder}} + F_{\text{pin}} \tag{31}$$

The force on the pin can be divided into two components: the force on the pin side surface caused by normal pressure and the frictional force on the pin tip surface caused by friction:

$$F_{\text{pin}} = F_{\text{pinside}} + F_{\text{pintip}} \tag{32}$$

In Fig. 9, the variations of the calculated tool forces with the transverse speeds are compared to Chen [25]. The error is only 4.4 %, which can validate the current model. As shown in Fig. 9, the frictional force on the shoulder contact surface

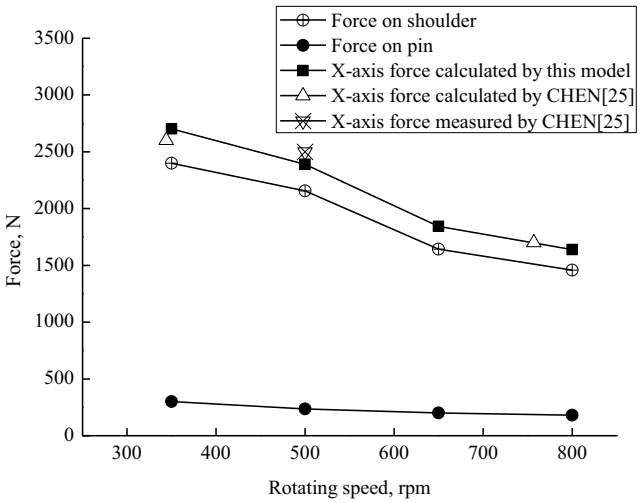

(a) *effect of rotating speed*

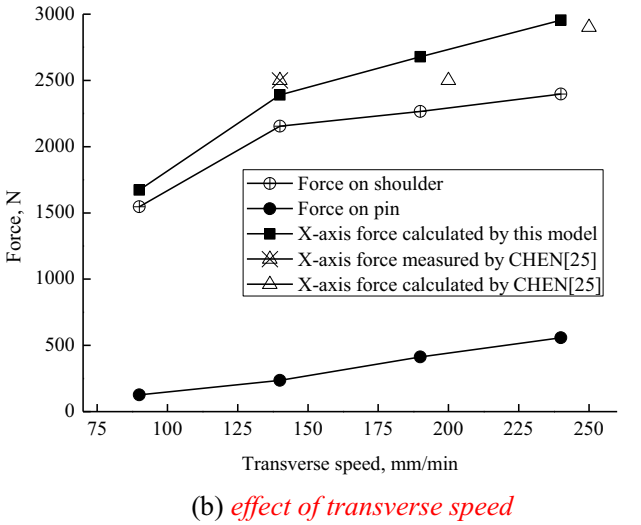

(b) *effect of transverse speed*

Fig. 9 Force on welding tool in different conditions. **a** Effect of rotating speed and **b** effect of transverse speed

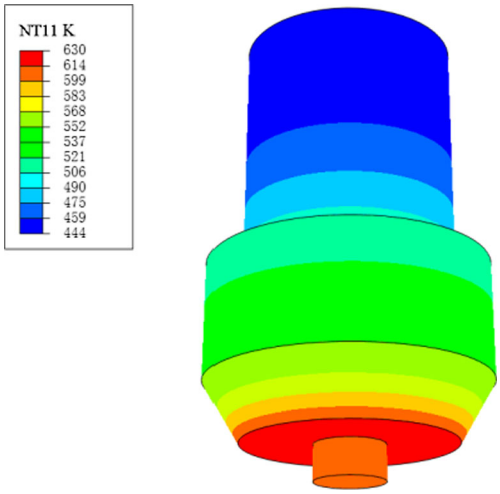

Fig. 10 Temperature distribution on the welding tool

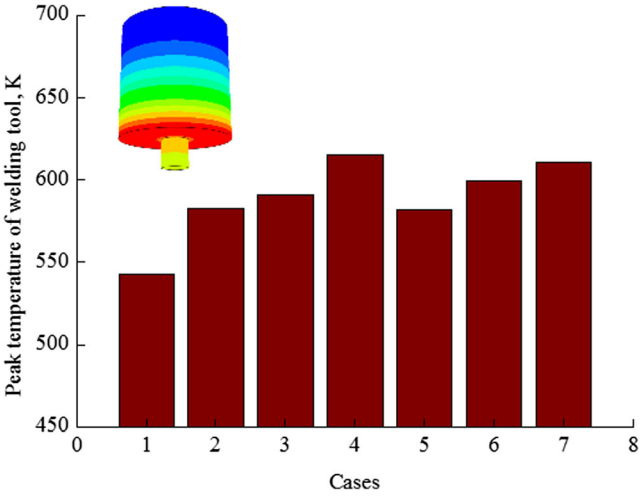

Fig. 12 Temperature distributions on the welding tool for seven cases

takes the main contribution to the tool force. The average ratio of $F_{shoulder}/F_x$ is 87.7 %, and the average ratio of F_{pin}/F_x is only 12.3 %.

As illustrated in Fig. 9a, the transverse force is decreased from 2701 to 1639 N, when the rotating speed is increased from 350 to 800 rpm. In Fig. 9b, the transverse force is increased from 1672 to 2954 N when the transverse speed is increased from 90 to 240 mm/min.

3.3 Fatigue stresses

The predicted temperature rises on the welding tool is shown in Fig. 10. The temperature distribution is identically the same to the one in [37]. The temperature along the axis of the welding tool is further compared, as shown in Fig. 11. The maximum difference is 9.3 %, which can validate the current model.

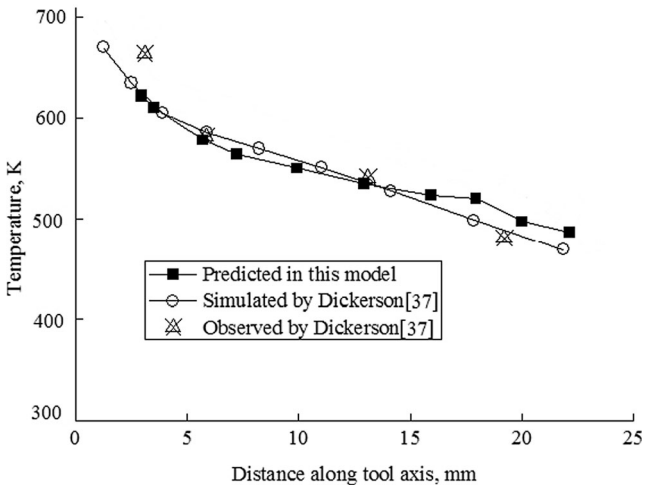

Fig. 11 Comparisons of temperatures on the welding tool

The temperature rises on the welding tool in seven different cases shown in Fig. 3 is given in Fig. 12. Temperature of the tool pins in seven cases is almost uniform. The maximum temperature rises with the increase in rotation speed and decreases when the transverse speed rises. The average temperature of the tool pin varies from 518 to 583 K in seven cases.

The computed tool forces in different cases are summarized in Table 3 for the calculation of the fatigue stress of the welding tool. The fatigue stresses calculated by finite element model, the analytical method 1 and the analytical method 2 are compared in Fig. 13. With comparison of the results from the finite element model, the maximum error of the analytical method 1 is 2.8 % and the maximum error of the analytical method 2 is 2.9 %, which can validate the proposed analytical methods for the computation of the fatigue stress of the welding tool.

It is obvious that the maximum fatigue stress occurs at the root of the pin. The schematic of the fatigue stress variations at the root of the pin is shown in Fig. 14. The maximum fatigue stress is decreased from 54.1 to 32.3 MPa when the rotating speed is increased from 350 to 800 rpm. However, the frequency of the alternating fatigue stress is equivalent to the

Table 3 Loads on tool pin

Cases	Pin force (N)	Tip force (N)
Case 1	230.4	71.0
Case 2	175.8	59.2
Case 3	145.2	56.5
Case 4	132.6	47.5
Case 5	90.0	35.4
Case 6	313.2	99.8
Case 7	417.6	139.6

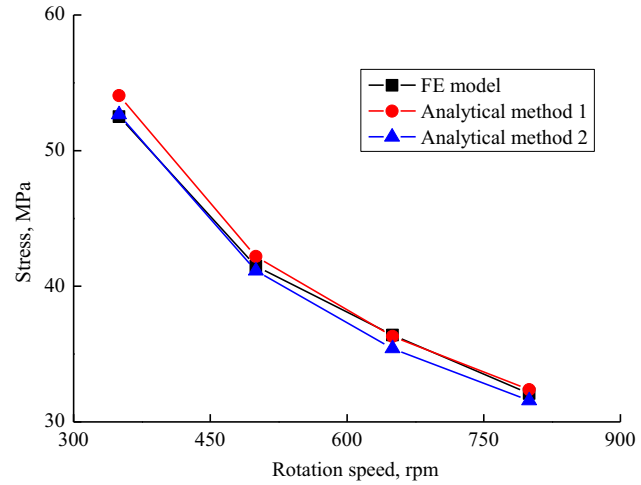

(a) *effect of rotating speed*

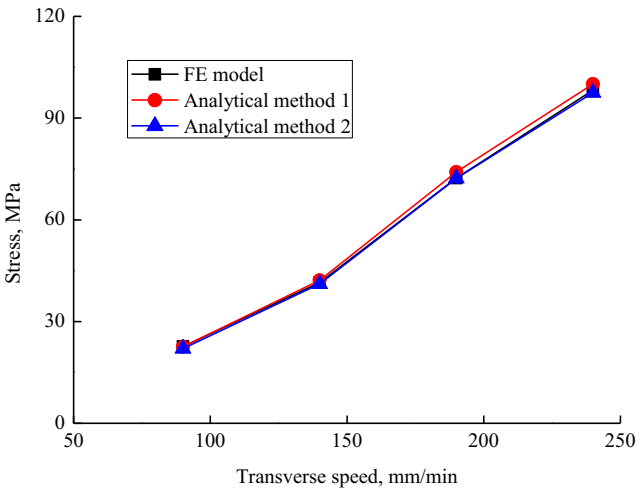

(b) *effect of transverse speed*

Fig. 13 Variations of fatigue stress with welding parameters. **a** Effect of rotating speed and **b** effect of transverse speed

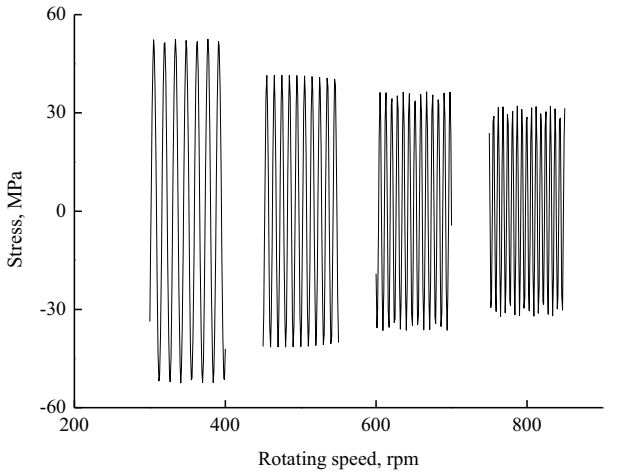

(a) *effect of rotating speed*

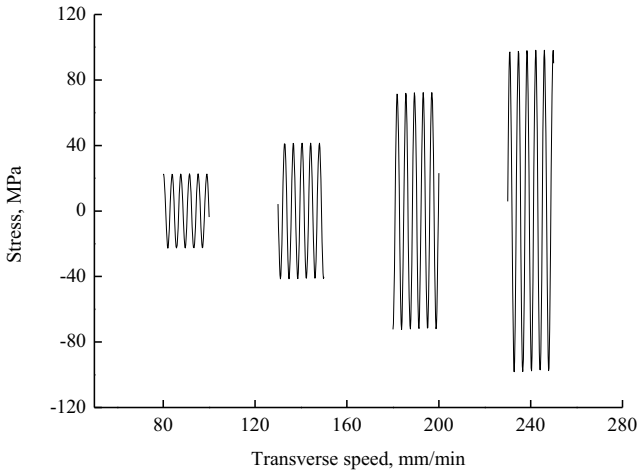

(b) *effect of transverse speed*

Fig. 14 Schematic of stress variations at the root of the pin. **a** Effect of rotating speed and **b** effect of transverse speed

rotating frequency. So, the increase of the rotating speed can also lead to the increase of the frequency of the fatigue stress. The maximum fatigue stress is increased from 22.7 to 98.2 MPa when the transverse speed is increased from 90 to 240 mm/min. The increase of the transverse speed can obviously lead to the increase of the fatigue stress on the welding tool while the frequency of the alternating fatigue stress keeps constant.

4 Conclusions

CFD model is used for the predictions of the tool forces in FSW. Then, two analytical methods are proposed for the calculations of the fatigue stress on the welding tool. The finite element model is used to validate the proposed analytical methods. The main obtained results are summarized as follows:

1. The transverse force of the tool consists of the frictional force on the shoulder contact surface, the frictional force on the pin tip surface, and the resistant force on the pin caused by the hydraulic pressure, in which the frictional force on the shoulder contact surface takes the main contribution.
2. The transverse force is decreased with the increase of the rotating speeds and is increased with the increase of the transverse speeds.
3. The maximum fatigue stress on the pin occurs at the root of the pin. Higher transverse speeds can lead to higher stresses on the pin.
4. The increase of the rotating speeds can lead to the decrease of the maximum fatigue stress on the pin and the increase of the frequency of the fatigue stress.

Acknowledgments This work was supported by Program for New Century Excellent Talents in University, the Fundamental Research Funds for the Central Universities, the National Natural Science Foundation of China (Nos. 11172057 and 11232003), the National Key Basic Research Special Foundation of China (2011CB013401), and the National High Technology Research and Development Program of China (2012AA050901).

References

1. Mishra RS, Ma ZY (2005) Friction stir welding and processing. Mater Sci Eng R 50:1–78
2. Gibson BT, Lammlein DH, Prater TJ, Longhurst WR, Cox CD, Ballun MC, Dharmaraj KJ, Cook GE, Strauss AM (2014) Friction stir welding: Process, automation, and control. J Manuf Process 16: 56–73
3. Nandan R, DebRoy T, Bhadeshia HKDH (2008) Recent advances in friction-stir welding—Process, weldment structure and properties. Prog Mater Sci 53:980–1023
4. Çam G (2011) friction stir welded structural materials: beyond al-alloys. Int Mater Rev 56:1–48
5. Çam G, Mıstıkoğlu S (2014) Recent developments in friction stir welding of al-alloys. J Mater Eng Perform 23:1936–1953
6. Sorensen CD, Stahl AL (2007) Experimental measurements of load distributions on friction stir weld pin tools. Metall Mater Trans B 38: 451–459
7. Kumar R, Singh K, Pandey S (2012) Process forces and heat input as function of process parameters in AA5083 friction stir welds. Trans Nonferrous Met Soc China 22:288–298
8. Mehta M, Chatterjee K, De A (2013) Monitoring torque and traverse force in friction stir welding from input electrical signatures of driving motors. Sci Technol Weld Join 18:191–197
9. Trimble D, Monaghan J, O'Donnell GE (2012) Force generation during friction stir welding of AA2024-T3. CIRP Annals-Manuf Technol 61:9–12
10. Balasubramanian N, Mishra RS, Krishnamurthy K (2011) Process forces during friction stir channeling in an aluminum alloy. J Mater Process Technol 211:305–311
11. Carlone P, Palazzo GS (2013) Influence of process parameters on microstructure and mechanical properties in AA2024-T3 friction stir welding. Metallogr Microstruct Anal 2:213–222
12. Zhang Z, Wan ZY (2012) Predictions of tool forces in friction stir welding of AZ91 magnesium alloy. Sci Technol Weld Join 17:495–500
13. Ulysse P (2002) Three-dimensional modeling of the friction stir-welding process. Int J Mach Tools Manuf 42:1549–1557
14. DebRoy T, De A, Bhadeshia HKDH, Manvatkar VD, Arora A (2012) Tool durability maps for friction stir welding of an aluminum alloy. Proc R Soc A 468:3552–3570
15. Arora A, Mehta M, De A, DebRoy T (2012) Load bearing capacity of tool pin during friction stir welding. Int J Adv Manuf Technol 61: 911–920
16. Soundararajan V, Zekovic S, Kovacevic R (2005) Thermo-mechanical model with adaptive boundary conditions for friction stir welding of Al 6061. Int J Mach Tools Manuf 45:1577–1587
17. Zhang Z, Zhang HW (2008) A fully coupled thermo-mechanical model of friction stir welding. Int J Adv Manuf Technol 37:279–293
18. Zhang Z, Wu Q, Zhang HW (2014) Numerical studies of effect of tool sizes and pin shapes on friction stir welding of AA2024-T3. Trans Nonferous Soc China 24:3293–3301
19. Assidi M, Fourment L, Guerdoux S, Nelson T (2010) Friction model for friction stir welding process simulation: calibrations from welding experiments. Int J Mach Tools Manuf 50:143–155
20. Dong P, Lu F, Hong JK, Cao Z (2001) Coupled thermomechanical analysis of friction stir welding process using simplified models. Sci Technol Weld Joining 6:281–287
21. Riahi M, Nazai H (2011) Analysis of transient temperature and residual thermal stresses in friction stir welding of aluminum alloy 6061-T6 via numerical simulation. Int J Adv Manuf Technol 55: 143–152
22. Colegrove PA, Shercliff HR (2005) 3-Dimensional CFD modelling of flow round a threaded friction stir welding tool profile. J Mater Process Technol 169:320–327
23. Zhang Z, Zhang HW (2014) Solid mechanics-based Eulerian model of friction stir welding. Int J Adv Manuf Technol 72:1647–1653
24. Arora A, Zhang Z, De A, DebRoy T (2009) Strains and strain rates during friction stir welding. Scripta Mater 61:863–866
25. Chen C, Kovacevic R (2004) Thermomechanical modelling and force analysis of friction stir welding by the finite element method. Proc IMechE Part C-J Mech Eng Sci 218:509–519
26. Neto DM, Neto P (2013) Numerical modeling of friction stir welding process: a literature review. Int J Adv Manuf Technol 65:115–126
27. Arora A, Debroy T, Bhadeshia HKDH (2011) Back-of-the-envelope calculations in friction stir welding—Velocities, peak temperature, torque, and hardness. Acta Mater 59:2020–2028
28. Arora A, Nandan R, Reynolds AP, Debroy T (2009) Torque, power requirement and stir zone geometry in friction stir welding through modeling and experiments. Scripta Mater 60:13–16
29. El-Tayeb NSM, Low KO, Brevern PV (2009) On the surface and tribological characteristics of burnished cylindrical Al-6061. Tribol Int 42:320–326
30. Devaraju A, Kumar A, Kotiveerachari B (2013) Influence of addition of Grp/Al2O3p with SiCp on wear properties of aluminum alloy 6061-T6 hybrid composites via friction stir processing. Trans Nonferrous Met Soc China 23:1275–1280
31. Timoshenko SP, Goodier JN (2004) Theory of elasticity. Tsinghua University Press, Beijing
32. Gere JM, Goodno BJ (2012) Mechanics of materials. CENGAGE Learning Custom Publishing, Boston
33. Martin HS (2009) Elasticity theory, applications, and numerics. Academic, Burlington
34. Wang MZ, Wang W, Wu JK (2002) Elasticity mechanics. Peking University Press, Beijing (In Chinese)
35. Focke AE (1990) Metals Handbook 9th ed. Properties and Selection: Irons and Steels, vol. 1. Materials Park, OH:ASM International
36. Zhang Z, Chen JT, Zhang ZW, Zhang HW (2011) Coupled thermo-mechanical model based comparison of friction stir welding process-es of AA2024-T3 in different thicknesses. J Mater Sci 46:5815–5821
37. Dickerson M, Shi QY, Shercliff HR (2003) Heat flow into friction stir welding tools. 4th International Symposium on Friction Stir Welding, Park City
38. Tang W, Guo X, McClure JC, Murr LE, Nunes A (1998) Heat input and temperature distribution in friction stir welding. J Mater Process Manuf Sci 7:163–172
39. Weglowski MS, Dymek S (2013) Relationship between friction stir processing parameters and torque, temperature and the penetration depth of the tool. Arch Civ Mech Eng 13:186–191